Nanoscale

PAPER

View Article Online
View Journal

Cite this: DOI: 10.1039/d5nr05037e

The role of nickel hydroxide phases in wastewater electrolysis for sustainable green hydrogen production

William Zitzmann,[a] Akhil S. Nair,[b] Beate Paulus,[b] Aran Rafferty,[c] Xuerui Yi,[d] Neil Robertson,[d] Caroline Kirk[d] and M. Veronica Sofianos *[a]

The energy sector plays a major role in driving climate change. Sustainable green hydrogen production through wastewater electrolysis is a promising alternative to fossil fuel consumption, without putting at risk precious resources, such as freshwater, at periods of high energy demand. This study investigates how interfacial engineering can be implemented in order to enhance the electrocatlytic activity of earth abundant nanostructures, such as nickel hydroxide, in water/wastewater electrolysis. It was demonstrated that the $Ni(OH)_2$ sample containing a mix of α- and β-phases phases (αβ1-$Ni(OH)_2$) exhibited the best oxygen evolution reaction (OER) performance due to the synergistic interface between the two phases, which enhanced its catalytic activity and reaction kinetics compared to single-phase samples. It showed a low Tafel slope of 18.8 mV dec^{-1} and potentials of 1.42, 1.63, and 1.82 V *vs.* RHE at current densities of 10, 100, and 500 mA cm^{-2}, respectively. This αβ1-$Ni(OH)_2$ sample was also tested for urea oxidation reaction (UOR). While UOR kinetics were slower (Tafel slope of 31.5 mV dec^{-1}), the potentials at 10 and 100 mA cm^{-2} (1.40 and 1.60 V *vs.* RHE) were slightly lower than those for OER, indicating higher energy efficiency at lower current densities. However, at 500 mA cm^{-2}, the UOR potential increased significantly to 2.20 V *vs.* RHE, compared to 1.82 V *vs.* RHE for OER, likely due to competition between UOR and OER at high current densities. Post-stability testing revealed surface degradation (cracking, sintering, oxidation, and oxygen defect formation) in OER conditions, while the same sample remained morphologically and chemically stable during UOR testing. This new knowledge provides valuable information into the design and interfacial engineering of $Ni(OH)_2$ nanostructures for wastewater electrolysis.

Received 29th November 2025,
Accepted 20th February 2026

DOI: 10.1039/d5nr05037e

rsc.li/nanoscale

Introduction

Decarbonising the energy sector with green hydrogen produced through wastewater electrolysis is a promising way to mitigate climate change.[1] This approach offers several advantages, as illustrated in Fig. 1: the energy-intensive oxygen evolution reaction (OER) can be replaced by the more favourable urea oxidation reaction (UOR), reducing the required potential from 1.23 V *vs.* RHE to 0.37 V *vs.* RHE; it avoids the use of freshwater, reducing vulnerability during droughts; it converts waste into valuable products such as hydrogen and nitrogen; and it prevents the formation of explosive H_2/O_2 mixtures by generating safer H_2/N_2 streams.[2–4] Before urea wastewater electrolysis can be realised for the sustainable production of green hydrogen, the sluggish six-electron UOR must be improved, as it is kinetically more demanding than the four-electron OER.[5] While precious metals like platinum and rhodium show excellent UOR activity, their cost and scarcity limit large-scale use.[6] Therefore, significant research is focused on developing affordable, efficient, and durable electrocatalysts based on earth-abundant transition-metal compounds.[7]

Recent studies have demonstrated that nickel (Ni) based electrocatalysts, and more specifically nickel hydroxides ($Ni(OH)_2$), are the most promising electrocatalysts for UOR among their other transition metal-based counterparts.[8] This high activity in enhancing the kinetics of the sluggish UOR is mainly attributed to the versatile $Ni(OH)_2$ structures and abundant 3d electrons in alkaline environments.

Strategies that have been implemented thus far for enhancing the electrocatalytic activity of $Ni(OH)_2$ towards the UOR have been namely: morphological design, heteroatom doping, surface vacancy formation, heterostructure development, and supporting materials utilisation.[8–12]

[a]School of Chemical and Bioprocess Engineering, University College Dublin, Belfield, Dublin 4, Ireland. E-mail: veronica.sofianos@ucd.ie
[b]Institut für Chemie und Biochemie, Freie Universität Berlin, Arnimallee 22, 14195 Berlin, Germany
[c]AMBER Research Centre, Naughton Institute, Trinity College Dublin, Dublin 2, D02PN40, Ireland
[d]School of Chemistry and EaStCHEM, University of Edinburgh, King's Buildings, David Brewster Road, Edinburgh, Scotland EH9 3FJ, UK

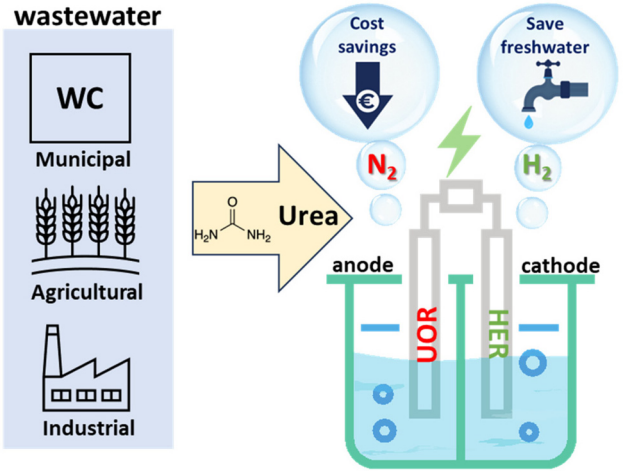

Fig. 1 Scenario of the UOR for sustainable green hydrogen production by utilising municipal, agricultural and industrial waste containing urea as feedstock to replace freshwater.

On the other hand, interfacial engineering of mixed-phase $Ni(OH)_2$ nanostructures is gaining considerable attention among the electrochemistry community, especially in the field of capacitor research, since these mixed-phase stuctures combine the distinct properties of the hexagonal crystal structure from the α and the layered one from the β phase. This combination creates a synergistic effect that enhances electrochemical performance by improving properties like conductivity, stability, and ion diffusion compared to single-phase Ni $(OH)_2$ [13] For example, Li *et al.* demostrated that the Al-substituted α/β-nickel hydroxide has higher electrochemical activity, better electrochemical reversibility, lower electrochemical resistance, and higher discharge voltage compared to the pure β-Ni $(OH)_2$.[14] Akhtar *et al.* showed that the cycling performance of the αβ-$Ni(OH)_2$ electrode demonstrated incredible capacity retention of 100% after 5000 continuous charge–discharge cycles at a current density of 50 mA cm^{-2}, with increased capacitance compared to beta-phase nickel hydroxide.[15] While, Yi *et al.* demostrated that αβ-$Ni(OH)_2$ exhibits excellent cycle stability, with 108% capacity retention after 2000 continuous charge–discharge cycles at 20 mA cm^{-1} in alkaline electrolyte, greater than pure phases of either α-$Ni(OH)_2$ or β-$Ni(OH)_2$.[16]

No previous studies have examined mixed-phase $Ni(OH)_2$ electrocatalysts for either or both the oxygen evolution reaction (OER) and the urea oxidation reaction (UOR), leaving a gap in understanding how the α and β phases influence activity in each process. Given the varying concentrations of urea in wastewater, there is a strong need for efficient bifunctional electrocatalysts capable of driving both reactions to enable stable, synergistic hydrogen production.[17–19] This study is the first to investigate how different phases of $Ni(OH)_2$ affect electrocatalytic performance in both OER and UOR. Four hydrothermally synthesised samples—α-$Ni(OH)_2$, β-$Ni(OH)_2$, and two mixed-phase materials (αβ1 and αβ2)—were evaluated. The mixed-phase αβ1-$Ni(OH)_2$ showed the highest OER activity and was further examined for UOR, where it also demonstrated superior performance. This enhancement is attributed to beneficial interfacial interactions between the α and β phases, highlighting interfacial engineering as a promising strategy to improve OER and UOR activity in $Ni(OH)_2$ and other transition-metal-based electrocatalysts.

M. Veronica Sofianos

M. Veronica Sofianos is a Materials Scientist with a PhD in Chemistry. She received a scholarship from the National Centre of Scientific Research (NCSR) "Demokritos" in Athens, Greece, to pursue doctoral research on nanomaterials for photocatalytic air purification. She later held a casual academic appointment at the University of Melbourne before joining Curtin University in Perth as a Research Fellow, where she focused on synthesising and characterising metal hydrides for hydrogen storage. She subsequently joined the UCD School of Chemical and Bioprocess Engineering as an Ad Astra Fellow, establishing her independent research career in advanced nanomaterials for sustainable energy applications.

Experimental

The detailed hydrothermal synthesis method of the $Ni(OH)_2$ samples is described in previous work reported by Yi *et al.*[16] and is illustrated in Fig. 2. In brief, pre-treated nickel foam (NF) pieces (1 cm × 3 cm) were placed in a Teflon lined autoclave together with nickel nitrate ($Ni(NO_3)_2{\cdot}6H_2O$, 3 mmol), urea (CH_4N_2O, 6 mmol) and ammonium fluoride (NH_4F) as an additive. The autoclave was then heated to 200 °C for 5 h as to obtain $Ni(OH)_2$ particles of the α, β and in-between phases

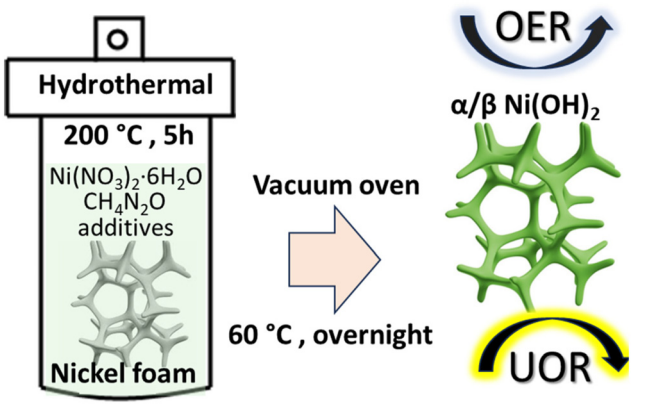

Fig. 2 Schematic illustration of the synthesis for the $Ni(OH)_2$ samples.

directly grown on the NF. Specifically, the α-$Ni(OH)_2$ phase was obtained with no ammonium fluoride additive. Whereas, aβ1-$Ni(OH)_2$, aβ2-$Ni(OH)_2$ and β-$Ni(OH)_2$ phases were synthesized using the molar ratios of ammonium fluoride to the nickel nitrate of 0.2 : 2 (aβ1-$Ni(OH)_2$), 0.5 : 2 (aβ2-$Ni(OH)_2$), and 4 : 2 (β-$Ni(OH)_2$), respectively. The samples were then washed and dried under vacuum overnight at 60 °C. The final mass loading of the $Ni(OH)_2$ phases on the NF was approximately 2 mg cm^{-2}.

All electrochemical experiments were conducted once at room temperature using an Autolab potentiostat (PGSTAT204 equipped with an FRA32M module, Metrohm) interfaced with a PC, running the Nova 2.1.7 software. A leakless Ag/AgCl reference electrode (3 M KCl, Metrohm) was employed, while a graphite rod (MW-4131, BASi) served as the counter electrode. The electrolytes used included a 1 M KOH aqueous solution (Sigma Aldrich, 90%) for OER, and a 1 M KOH (Sigma Aldrich, 90%) mixed with 0.33 M urea (NH_2CONH_2, Sigma Aldrich, ≥99.5%) aqueous solution for UOR. Both electrolytes were at pH 14. Alkaline electrolytes, typically 1 M KOH with 0.33 M urea, are most commonly used for electrochemical urea oxidation reactions (UOR) due to the following reasons: (1) 0.33 M reflects the typical urea concentration found in urine, making it relevant for practical applications; (2) deviations from this concentration—either higher or lower—can affect UOR kinetics by altering the diffusion behaviour of reactants and intermediates.[20,21] RuO_2 (99.9%, Sigma Aldrich) was employed as reference catalysts for OER benchmarking. To prepare the RuO_2 electrode, a homogenous ink was formulated containing 5 mg of RuO_2 powder, 490 μL of distilled water, 490 μL of absolute ethanol, and 20 μL of 5% Nafion (Sigma Aldrich). The ink was homogenised in an ultrasonic bath for 20 minutes. 10 μL of the as-prepared homogenous ink was drop-cast using a micropipette onto a 5 mm glassy carbon (GC) rotating disk electrode from Metrohm, which served as the working electrode. The drop-cast ink was left to dry under an IR lamp. The surface area of the glassy carbon working electrode was 0.2 cm^2, with a total load of electrocatalyst powder equal to 0.05 mg. During all electrochemical measurements, the working electrode was rotated at 3000 rpm by a rotation unit (Metrohm) to eliminate bubbles. The surface area of the $Ni(OH)_2$ working electrodes was 5 mm × 5 mm (0.25 cm^2), comparable to the GC's surface area. All potentials were converted to the reversible hydrogen electrode (RHE) scale using the equation: $E_{RHE} = E_{Ag/AgCl} + 0.197 + 0.059 \times pH$. E_{RHE} is the measured potential *versus* the RHE, $E_{Ag/AgCl}$ is the measured potential against the Ag/AgCl (3 M KCl) reference electrode, 0.197 V is the standard potential of Ag/AgCl (3 M KCl) at 25 °C, and 0.059 V is the Nernstian slope per pH unit. Linear sweep voltammetry (LSV) was performed at a scan rate of 5 mV s^{-1} under a nitrogen atmosphere (>99.999%, BOC) to evaluate the OER and UOR activities of the $Ni(OH)_2$ samples. Tafel slopes were derived from the polarisation curves by plotting the logarithm of the current density against the overpotential. Electrochemical impedance spectroscopy (EIS) measurements were conducted at the determined open-circuit potential using a 10 mV AC amplitude across a frequency range of 100 kHz to 1 Hz. The uncompensated resistance (R_s) was defined from Nyquist plots (Fig. S1 for 1 M KOH and S5 for 1 M KOH + 0.33 M Urea) and used to correct for ohmic drop using: $E_c = E_e - iR_s$ where E_c is the corrected potential and E_e is the experimental potential (Table S1 in 1 M KOH and S3 in 1 M KOH + 0.33 M Urea). The LSV raw data with no iR_s correction is presented in the SI section (Fig. S2 in 1 M KOH and S6 in 1 M KOH + 0.33 M urea). The stability of the best performing $Ni(OH)_2$ sample was assessed by chronoamperometry over 24 hours. Cyclic voltammetry (CV) was used to estimate the electrochemically active surface area (ECSA) of each sample. CV measurements were carried out at varying scan rates (20, 40, 60, 80, 100, and 120 mV s^{-1}) within the non-faradaic region (0.83–1.23 V *vs.* RHE). The difference in anodic and cathodic current densities (Δj) at 1.026 V (*vs.* RHE) was plotted against the scan rates, and the slope obtained from the linear fit, when multiplied by the electrode surface area, yielded the double-layer capacitance (C_{dl}). A specific capacitance of 40 μF cm^{-2} was used for a flat surface at pH 14 to calculate the ECSA using the formula: ECSA = $C_{dl}/(40\ \mu F\ cm^{-2})\ cm^2$.

Nitrogen gas adsorption/desorption measurements were carried out at 77 K using a Nova 2400e surface area analyser (Quantachrome, UK) to assess the specific surface area and macro-mesoporosity of the $Ni(OH)_2$ samples. The specific surface area was determined using the Brunauer–Emmett–Teller (BET) multi-point method, analysing adsorption data within the relative pressure range of 0.05 to 0.30.[22] Pore size distributions and volumes within the mesoporous (2–50 nm) and macroporous (>50 nm) ranges were evaluated using the Barrett–Joyner–Halenda (BJH) method, derived from the desorption branch of the isotherms.[23] Prior to measurement, all samples were degassed under vacuum at 150 °C for 4 hours.

Morphological analysis before and after OER and UOR chronoamperometry testing was conducted using a Zeiss Sigma 300 scanning electron microscope (SEM). Prior to imaging, the best performing $Ni(OH)_2$ sample was mounted onto an aluminium stub using carbon tape and coated with a 4 nm layer of platinum to reduce charging effects during SEM imaging. Whereas, the surface chemistry of the $Ni(OH)_2$ sample before as well as after OER and UOR chronoamperometry stability testing, was examined using a Kratos AXIS Ultra DLD X-ray Photoelectron Spectrometer (XPS) under ultra-high vacuum conditions with an Al-Kα X-ray source (1486.7 eV). The acquired data were analysed using Casa XPS software, with calibration performed using the adventitious surface C 1s peak set at 284.5 eV.

The density functional theory (DFT) calculations were performed on the bulk phases without taking into consideration any surface defects, by applying the all-electron code FHI-aims with numeric atom-centred orbital (NAO) basis sets.[24] The standard "light" basis sets were used with zero-order regular approximation to account for the relativistic effects. A *k*-grid density of 5 $Å^{-1}$ was applied to sample the Brillioun zone. The structural optimizations were performed using the Perdew–Burke–Ernzerhof (PBE) functional under the generalized gradi-

ent approximation (GGA).[25] The dispersion interactions were accounted by non-local many body dispersion (MBD) method, as implemented in FHI-aims.[26] For the electronic structure calculations, Heyd–Scuseria–Ernzerhof (HSE) functional with a Hartree–Fock exchange of 25% (HSE06) was used.[27] Spin-polarized calculations were performed for all structures.

Results and discussion

The water electrolysis performance of the $Ni(OH)_2$ samples was first evaluated in 1 M KOH against the OER, and is presented in Fig. 3. All four $Ni(OH)_2$ samples surpassed RuO_2 in OER activity, achieving high current densities in the range of 700 to 800 mA cm^{-2} (Fig. 3a), showcasing their great potential for industrial use. Industrial electrolysers often require >500 mA cm^{-2} current densities for the generation of hydrogen and oxygen gas.[28] In detail, the αβ1-$Ni(OH)_2$ sample demonstrated the highest OER performance, exhibiting the smallest Tafel slope equal to 18.8 mV dec^{-1} (Fig. 3b), along with a potential of 1.42 V *vs.* RHE at 10 mA cm^{-2}, 1.63 V *vs.* RHE at 100 mA cm^{-2}, and 1.82 V *vs.* RHE at 500 mA cm^{-2} (Fig. 3c). Its small value of Tafel slope means that the αβ1-$Ni(OH)_2$ sample exhibited the fastest reaction kinetics in OER in comparison to the other three $Ni(OH)_2$ samples, whereas its small overpotential values in the above mentioned current densities indicates that the required energy to overcome the kinetic barriers to run the OER is smaller in comparison to the other samples.[29] Both of these traits (a small Tafel slope value and a small overpotential at a current density higher than 500 mA cm^{-2}) are desired when designing electrocatalysts for industrial green hydrogen production. The second-best performing sample in relation to overall activity was the αβ2-$Ni(OH)_2$ (Fig. 3a), exhibiting a Tafel slope of 116.5 mV dec^{-1} (Fig. 3b), and an potential of 1.51, 1.64, and 1.86 V *vs.* RHE for 10, 100 and 500 mA cm^{-2}, respectively (Fig. 3c). Even though this sample showed the second-best overall performance in OER activity when compared to the single phase $Ni(OH)_2$ samples (α-$Ni(OH)_2$, and β-$Ni(OH)_2$), it demonstrated the highest value of Tafel slope, showing that the reaction kinetics of the OER are slow. On the other hand, though, the energy required to overcome the kinetic barriers to initiate the reaction are low since the recorded overpotentials

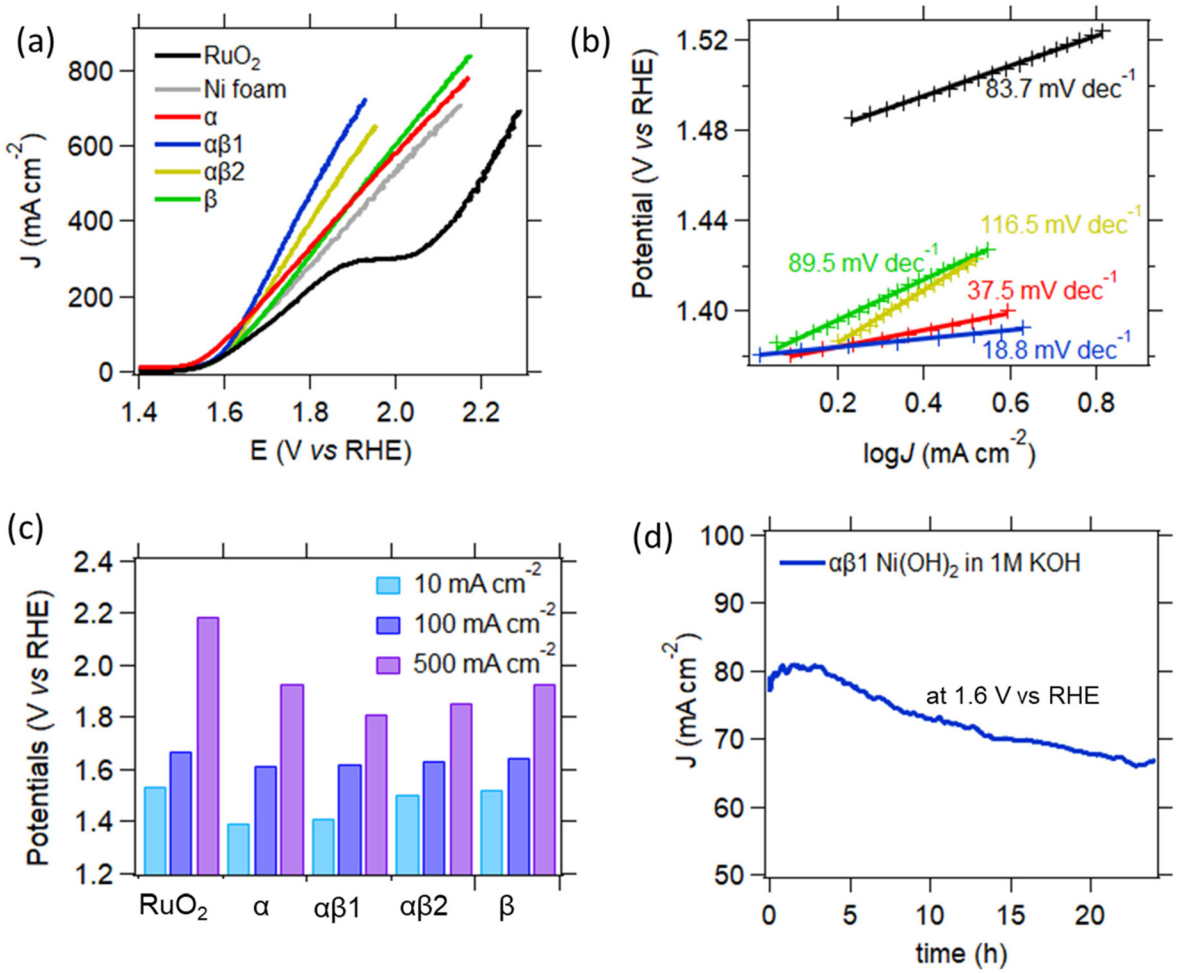

Fig. 3 OER performance of the $Ni(OH)_2$ samples. (a) polarization curves, (b) Tafel slopes, (c) potentials at 10, 100 and 500 mA cm^{-2}, (d) chronoamperometric curve of αβ1-$Ni(OH)_2$ at 1.6 V (*vs.* RHE) for 24 h.

for current densities as high as 500 mA cm^{-2} were low in value when compared to the single-phase $Ni(OH)_2$ samples. Both α-$Ni(OH)_2$, and β-$Ni(OH)_2$ samples exhibited very similar overall performance (Fig. 3a), with the α-$Ni(OH)_2$ sample having both a smaller Tafel slope (37.5 mV dec^{-1} (Fig. 3b)) and smaller potentials at 10, 100 and 500 mA cm^{-2} equal to 1.40, 1.62, and 1.94 *vs.* RHE than the β-$Ni(OH)_2$ sample. Specifically, β-$Ni(OH)_2$ demonstrated a Tafel slope equal to 89.5 mV dec^{-1} (Fig. 3b) and an overpotential of 1.53 V *vs.* RHE at 10 mA cm^{-2}, 1.65 V *vs.* RHE at 100 mA cm^{-2}, and 1.93 V *vs.* RHE at 500 mA cm^{-2}. A proposed OER mechanisms in 1 M KOH is as follows.[30] OH* are first generated, and then O* and *OOH intermediate species are formed subsequently as described below, * donates surface bound species.

$$OH^- + * \rightarrow OH* + e^- \quad (1)$$

$$OH* + OH^- \rightarrow O* + H_2O + e^- \quad (2)$$

$$O* + OH^- \rightarrow *OOH + e^- \quad (3)$$

$$*OOH + OH^- \rightarrow * + O_2 + H_2O + e^- \quad (4)$$

(2) Finally, two adsorbed oxygen atoms combine to produce oxygen.

$$O* + O* \rightarrow O_2 \quad (5)$$

To relate the electrocatalytic activity of the $Ni(OH)_2$ samples to their physicochemical properties, nitrogen adsorption/desorption analysis was conducted together with cyclic voltammogram for determining their ECSA and C_{dl}. All four $Ni(OH)_2$ samples are consisted of ultrathin $Ni(OH)_2$ nanosheets, approximately 1–2 nm thick, directly grown on the NF, as shown in Fig. 4(a and b) for the αβ1-$Ni(OH)_2$ sample, and reported by Yi *et al.*[16] The NF sample was unsuitable for full isotherm analysis as it was not sufficiently porous within the range of the instrument. However, the samples with grown nanosheet coverage were amenable to full analysis. Differences in the specific surface area across the four samples as well as their average pore diameter and pore volume, as presented in Table 1, can be attributed to the degree of nanosheet packing grown on the NF, as well as subtle differences between the nanosheets themselves. In detail, sample α-$Ni(OH)_2$ exhibited the highest specific surface of 16.8 m^2 g^{-1}. The sample with the second highest specific surface area was αβ2-$Ni(OH)_2$ with 8.3 m^2 g^{-1}, followed by sample αβ1-$Ni(OH)_2$ with 4.1 m^2 g^{-1} and last β-$Ni(OH)_2$ with 3.9 m^2 g^{-1}. The average pore size values range from 11.0 to 17.6 nm, with their BJH pore size distributions presented in Fig. S3. The α-$Ni(OH)_2$ sample exhibited the smallest pore size of 11 nm, followed by samples αβ2-$Ni(OH)_2$ and β-$Ni(OH)_2$ with 13.4 nm and finally sample αβ1-$Ni(OH)_2$ with 17.6 nm. Although samples αβ2-$Ni(OH)_2$ and β-$Ni(OH)_2$ demonstrated the same average pore size, the total pore volume of the αβ2-$Ni(OH)_2$ sample is more than double that of β-$Ni(OH)_2$, meaning that a higher percentage in porosity is present in the former. The sample with the lowest total pore volume was αβ1-$Ni(OH)_2$. Samples α-$Ni(OH)_2$, αβ2-Ni

Table 1 Specific surface area, average pore size, and total pore volume of $Ni(OH)_2$ samples

Electrocatalyst powder	Specific surface area (m^2 g^{-1})	Total pore volume (cm^3 g^{-1})	Average pore diameter (nm)
Ni foam	0.7	—	—
α-$Ni(OH)_2$	16.8	0.050	11.0
αβ1-$Ni(OH)_2$	4.1	0.019	17.6
αβ2-$Ni(OH)_2$	8.3	0.027	13.4
β-$Ni(OH)_2$	3.9	0.012	13.4

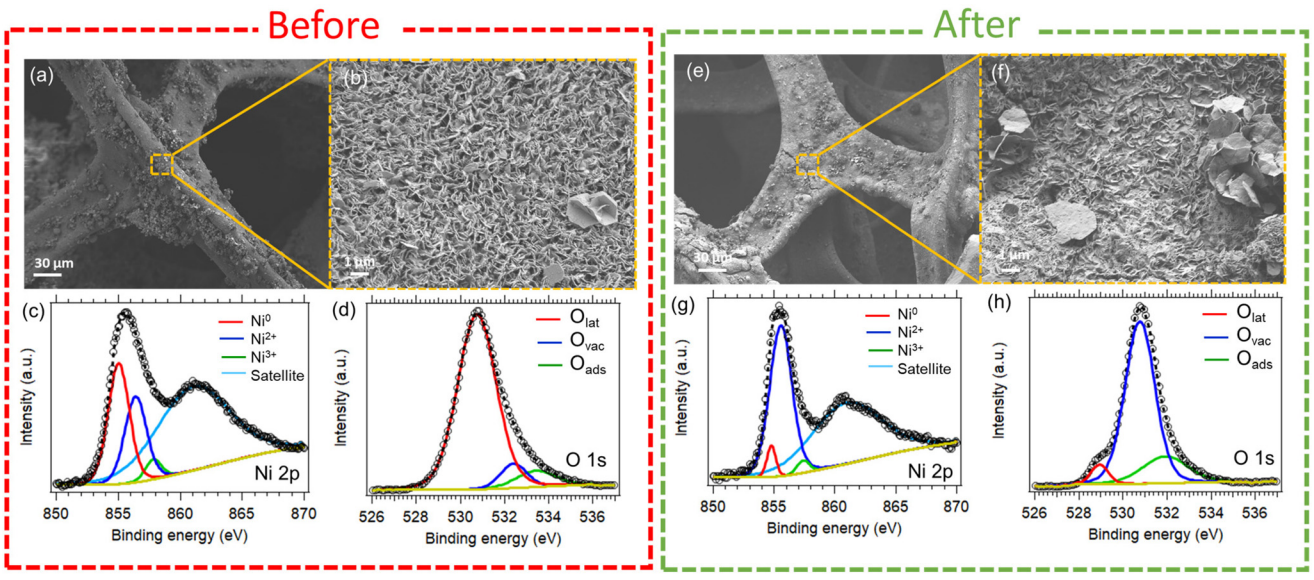

Fig. 4 SEM micrographs of the (a, b, e and f) αβ1-$Ni(OH)_2$ sample, together with its high resolution XPS spectra of (c and g) nickel and (d and h) oxygen before and after OER chronoamperometry measurements.

$(OH)_2$ and β-$Ni(OH)_2$, exhibited very similar ECSA values of ~24 cm^2 and C_{dl} values of 0.9 mF (Table S2), with the following trend α-$Ni(OH)_2$ > αβ2-$Ni(OH)_2$ > β-$Ni(OH)_2$. The αβ1-$Ni(OH)_2$ sample exhibited the lowest ECSA and C_{dl} values equal to 18.98 cm^2 and 0.76 mF, respectively. It is worth noting that, even though αβ1-$Ni(OH)_2$ exhibited the smallest values in specific surface area, ECSA and C_{dl}, it demonstrated the highest catalytic activity in the OER, showing that surface chemistry manipulation through interfacial engineering is a good strategy to enhance the electrocatalytic activity of catalysts by optimising the intermediate active species' adsorption energy, and improve the reaction kinetics.[31] Quantification of the α and β phases using X-ray powder diffraction (XRPD) could not be carried out for the αβ1- and αβ2-$Ni(OH)_2$ samples, as their structures are ill-defined and any phase-quantification analysis by XRPD would result in large errors in the calculated proportions. However, to provide a rough estimation of the phase composition in these mixed-phase samples, we used thermogravimetric analysis (TGA) results reported previously for this system by Yi *et al.*[16] Considering that the conversion of $Ni(OH)_2$ to NiO above 250 °C involves loss of H_2O, any additional mass losses originate from the species located between the layers of $Ni(OH)_2$, which correspond to the fraction of material assigned to the α phase. Based on this approach, αβ1-$Ni(OH)_2$ contains 76% α phase, and αβ2-$Ni(OH)_2$ contains 12% α phase.

The best performing sample, αβ1-$Ni(OH)_2$, was selected for stability testing by performing chronoamperometry measurements at 1.6 V *vs.* RHE (80 mA cm^{-2} corresponding current density) for 24 h. A continuous drop in the current density is observed throughout the 24 h measurement that totals to a 12.5% drop overall. In order to understand the root of this drop in current density over the 24 h period, we performed SEM imaging on the αβ1-$Ni(OH)_2$ as well as XPS analysis before and after stability testing (Fig. 4), in order to track both morphological and chemical changes that may have taken place on the electrode's surface. From the SEM micrographs before chronoamperometry (Fig. 4a and b) it can be observed that $Ni(OH)_2$ plates are directly grown on the NF which are approximately 1–2 nm thick as also reported by Yi *et al.*[16] After chronoamperometry testing the morphology of the αβ1-$Ni(OH)_2$ has remained the same but sintering of the plates is very evident as well as cracking throughout the surface of the electrode. These morphological changes on the electrode's surface can explain the decline in activity since less surface area is actively participating in water electrolysis. The cause of the sintering may be attributed to the harsh operating conditions of the stability testing such as the strong alkaline environment from the electrolyte and the high potential. The high resolution XPS spectra of nickel and oxygen of the same sample is presented in Fig. 4c and d, respectively. It can be seen that four peaks are present in Fig. 4c with Ni0 located at 855 eV originating from the Ni foam, Ni^{2+} positioned at 856.4 eV, and N^{3+} situated at 857.8 eV. A satellite peak is located at 861 eV. Taking into consideration the area of each deconvoluted peak, we can assign 23.71% to Ni0, 17.29% to Ni^{2+}, 2.96% to Ni^{3+}, and 46.04% to the satellite peak. Meanwhile, the high-resolution oxygen spectra shown in Fig. 4d, reveals three oxygen peaks. In detail, the first peak at 530.7 eV is attributed to the oxygen lattice in the $Ni(OH)_2$ crystal structure corresponding to 83.91%. The second peak at 532.4 eV is assigned to the oxygen vacancies, equivalent to 8.06% of the total spectra, and the third peak at 533.4 eV is due to the absorbed oxygen on the αβ1-$Ni(OH)_2$ sample which corresponds to 8.03%. After chronoamperometry testing, the area of Ni^0 decreased down to 3.42% with a peak maximum at 854.8 eV, whereas the peak area of Ni^{2+} increased to 41.95% (from 17.23%) with peak location at 855.5 eV. The presence of Ni^{3+} species on the electrode's surface remained relatively constant with a peak area equal to 1.89% and the same peak position before the stability testing at 857.4 eV. In addition, an increase in the semi-quantitative oxygen vacancies (for definitive quantification of oxygen vacancy analysis Electron Paramagnetic Resonance is required) was observed with the corresponding peak areas being 75.78% with peak position at 530.7 eV, together with an increase in the adsorbed oxygen to 18.95% with peak position at 531.9 eV. The percentage of the oxygen lattice decreased down to 5.27% with an allocated peak position at 528.9 eV. The observed chemical shift to lower binding energies (lower eV) for both the nickel and oxygen species on the electrode's surface can be attributed to the increase in electron density around the atom, making the core electrons easier to remove. This shift commonly occurs when an atom is in a more reduced chemical state, bonded to more electropositive elements, or has experienced electron donation into its electronic orbitals.[32]

To explore the potential of the best performing αβ1-$Ni(OH)_2$ sample in wastewater electrolysis, UOR measurements were performed in urea containing alkaline pure water, and were compared against the activity in alkaline pure water (Fig. 5). The rationale for selecting the best OER-performing sample for further UOR evaluation is based on the well-established understanding that both OER and UOR are governed by the same active sites. Specifically, the ability of $Ni(OH)_2$ to undergo the Ni^{2+}/Ni^{3+} redox transition and form catalytically active NiOOH species.[33–35] Consequently, electrocatalysts that exhibit high activity for the OER are generally expected to show a similar performance trend for the UOR. As can be observed in Fig. 5a, the αβ1-$Ni(OH)_2$ sample showed enhanced UOR performance at current densities lower than 100 mA cm^{-2}, whereas at higher current densities (>100 mA cm^{-2}) the same sample exhibited better OER performance. The UOR kinetics were slower in comparison to the OER, with the αβ1-$Ni(OH)_2$ sample exhibiting a Tafel slope equal to 31.5 mV dec^{-1} for UOR and 18.8 mV dec^{-1} for OER. It is worth noting that the potential for UOR at 10 and 100 mA cm^{-2} current densities was 1.40 and 1.60 V *vs.* RHE respectively, in comparison to 1.42 and 1.63 V *vs.* RHE for OER correspondingly. Meaning that less energy is required to run the UOR at those values of current density in comparison to OER. The same cannot be said for current densities higher than 100 mA cm^{-2}, as the potential of the αβ1-$Ni(OH)_2$ sample at 500 mA cm^{-2} was 2.20

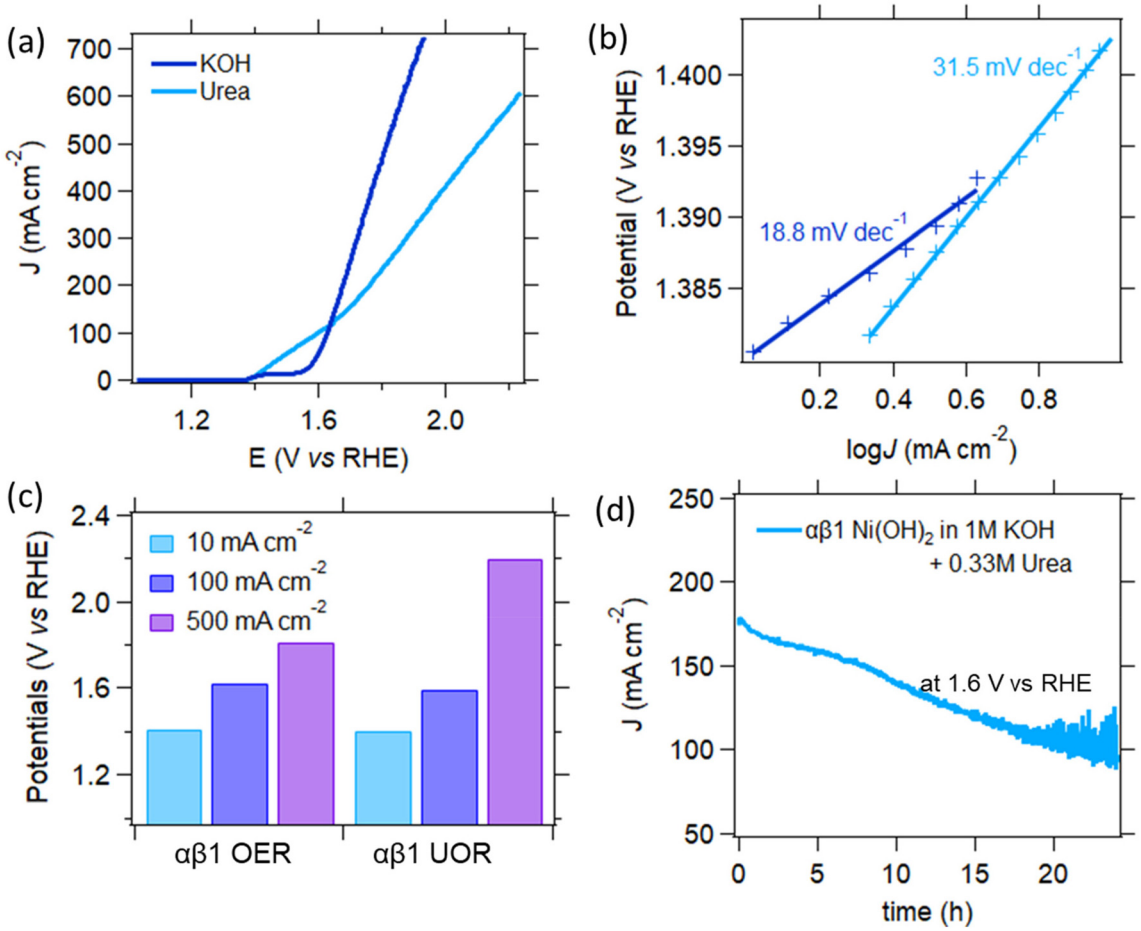

Fig. 5 OER and UOR performance of the αβ1-$Ni(OH)_2$ sample. (a) polarization curves, (b) Tafel slopes, (c) overpotentials at 10, 100 and 500 mA cm^{-2}, (d) UOR chronoamperometric curve at 1.6 V (*vs.* RHE) for 24 h.

V *vs.* RHE, whereas for OER it was 1.82 V *vs.* RHE for the same current density. One would expect the overpotentials for running the UOR to be much lower than those for OER, but in reality, as mentioned in the literature, UOR requires such high energy to overcome the activation barrier that, in practice, it has similar energy requirements as the OER.[36] In addition, regarding the potential-dependent reaction mechanism and product distribution, the UOR on Ni-based catalysts in alkaline media faces strong competition from the OER once the applied potential surpasses the OER overpotential (typically around 1.5 V *vs.* RHE).[34,37,38] This competition likely arises because both reactions utilize the same or similar active species, resulting in the formation of O_2 as a by-product, which decreases UOR efficiency and compromises catalyst stability. This competition between UOR and OER stems from OH^- adsorption.[34] While moderate OH^- adsorption promotes the sequence of proton-coupled electron transfer reactions needed to break the C–N bond in urea and drive the UOR, excessive OH^- adsorption hinders urea adsorption on active sites and intensifies OER competition. The chronoamperometry measurements showed a constant decline in stability over a 24 h period, with a local instability in the current density being noticed after 15 h which is caused by trapped bubbles on the electrode's surface as observed during the measurement. To further understand the long-term effect of UOR on the electrode's surface after its stability testing, SEM and XPS analysis were conducted on the αβ1-$Ni(OH)_2$ sample. As noticed in Fig. 6a and b, no evident morphological changes took place on the electrode's surface when taking into consideration the initial morphological micrographs of the same sample presented in Fig. 4a and b. In addition, XPS analysis of the high-resolution spectra of Ni and O showed no evidence of surface oxidation and oxygen defect formation after chronoamperometry. In detail, the calculated peak area that corresponds to metallic Ni^0 was 36.5% with peak position at 855.1 eV. The Ni^{2+} peak area was calculated to be 7.97% with peak position at 856.3 eV, and Ni^{3+} was equal to 5.10% with peak position at 857 eV. The area of the satellite peak was 50.44%, positioned at 861.2 eV. The concentration of the oxygen lattice as calculated by its peak area was equal to 90.83% with a peak position at 530.7 eV. The peak assigned to the presence of oxygen vacancies was 4.97% with 532.1 eV peak position. Whereas, oxygen peak area that corresponds to adsorbed oxygen was equal to 4.20% with peak position at 861.2 eV.

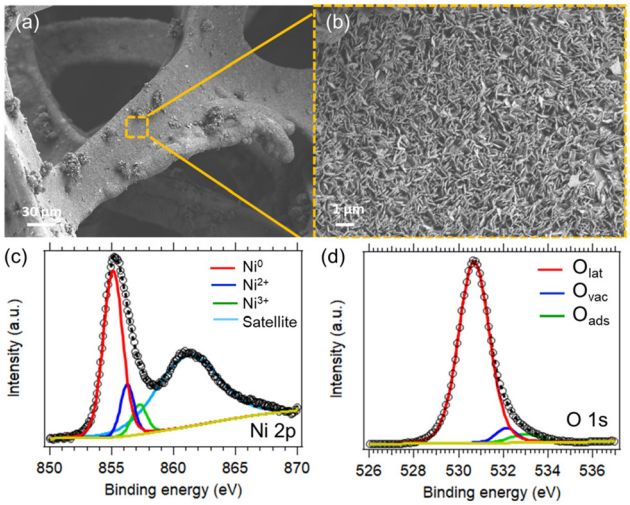

Fig. 6 SEM micrographs of the (a and b) αβ1-$Ni(OH)_2$ sample, together with its high resolution XPS spectra of (c) nickel and (d) oxygen after UOR chronoamperometry measurements.

Botte *et al.*[4,39,40] suggested two potential pathways for the UOR for $Ni(OH)_2$ samples. One of these is the indirect oxidation mechanism, also referred to as the electrochemical–chemical oxidation (EC0) mechanism. In this process, $Ni(OH)_2$ is initially electrochemically converted to NiOOH. The NiOOH then chemically oxidizes urea, producing N_2 and CO_2, and is itself chemically reduced back to $Ni(OH)_2$. Finally, $Ni(OH)_2$ reacts with OH^- ions in the electrolyte to regenerate the active NiOOH species. The process is as follows.

$$6Ni(OH)_2 + 6OH^- \leftrightarrow 6NiOOH + 6H_2O + 6e^- \quad (6)$$

$$6NiOOH + CO(NH_2)_2 + H_2O \rightarrow 6Ni(OH)_2 + N_2 + CO_2 \quad (7)$$

$$CO(NH_2)_2 + 6OH^- \rightarrow N_2 + 5H_2O + CO_2 + 6e^- \quad (8)$$

The second pathway is the direct electrochemical oxidation mechanism, in which the NiOOH intermediate directly adsorbs urea molecules and reacts with OH^- ions in the electrolyte, leading to the formation of N_2 and CO_2. The process is described below.[41]

$$Ni(OH)_2 + OH^- \leftrightarrow NiOOH + H_2O + e^- \quad (9)$$

$$CO(NH_2)_2 + 6OH^- \rightarrow N_2 + 5H_2O + CO_2 + 6e^- \quad (10)$$

Taking into consideration the XPS analysis of the high-resolution Ni and O spectra before and after chronoamperometry testing which showed no further oxidation of the electrode's surface or oxygen vacancy formation after stability testing, together with literature studies in which operando Raman spectroscopy was conducted during UOR showing simultaneous occurrence of electrochemical oxidation of $Ni(OH)_2$ to NiOOH and the chemical reduction of NiOOH by urea; indicates that the catalytic mechanisms for the UOR is electrochemical–chemical oxidation (EC0) mechanism.[4] In addition, a few studies have recently reported that the active species of Ni-based catalysts may not be Ni^{3+}, but Ni^{2+} as in our study. For instance, Li *et al.*[42] developed a novel Ru–Co DAS/NiO heterostructure. Using operando electrochemical impedance spectroscopy (EIS) and Raman spectroscopy, they showed that the UOR on Ru–Co DAS/NiO initiates before the conversion of Ni^{2+} to Ni^{3+}. This catalyst demonstrated outstanding UOR performance, achieving 10 mA cm^{-2} at a potential of just 1.288 V *vs.* RHE and maintaining stability for up to 330 hours.

While the αβ1-$Ni(OH)_2$ sample demonstrated high current densities (>500 mA cm^{-2}) in both OER and UOR compared to other recent state-of-the-art Ni-based electrocatalysts (Table S4), translating this performance to practical wastewater electrolysis systems requires consideration of several scalability challenges. Real wastewater contains competing species, variable pH, and fluctuating urea concentrations, all of which may reduce long-term activity and selectivity.[43] Electrocatalysts durability under continuous operation, resistance to poisoning or surface fouling, and mechanical stability when integrated into large-area electrodes are also critical factors. Moreover, scaling hydrothermal synthesis to industrially relevant quantities may require process optimisation or alternative fabrication methods.[44] Finally, system-level challenges, such as managing mass transport limitations, ensuring efficient gas separation, and minimising energy losses, must be addressed for commercial deployment.

To further understand the structural and electronic properties of $Ni(OH)_2$ structures linked with their electrocatalytic activity, DFT calculations were carried out. Though the experimental studies revealed that the mixed αβ1-$Ni(OH)_2$ phase is the most reactive, the exact interface between the α and β phases in this sample is not structurally known, and hence we have limited our computational studies to the parent α, β phases. The structural optimisations of α-$Ni(OH)_2$ and β-$Ni(OH)_2$ were performed based on the experimental CIF files (Fig. 7a and 1b). Since the positions of H atoms were not known for the α- $Ni(OH)_2$ from the experimental CIF files, we have tried multiple H-atom arrangements and considered the most stable structure for the further calculations.

For the β-$Ni(OH)_2$ structure, the DFT-relaxed lattice constants are in close agreement with the experimentally observed values whereas for the α-$Ni(OH)_2$ structure, a lattice contraction along the z-direction is observed. This can be attributed to the fact that under the experimental conditions, α-$Ni(OH)_2$ contains additional molecules (*e.g.* H_2O, nitrate) between the $Ni(OH)_2$ layers. To account for this, we re-optimized the α-$Ni(OH)_2$ structure with water molecules intercalated between the $Ni(OH)_2$ layers. The resulting structure (Fig. 8c) has lattice constants a = 3.231, b = 3.1, c = 22.263 Å, indicating strong agreement with the experimental lattice constants without any contraction along the z-direction as observed in the α-$Ni(OH)_2$ structure without intercalated H_2O molecules. The stability of this structure against such a deformation can be understood by the strong hydrogen bonding between the –OH groups of Ni$(OH)_2$ units and the H_2O molecules. There are three pronounced hydrogen bonds per intercalated water molecule with a bond distance between 1.70 and 1.83 Å.

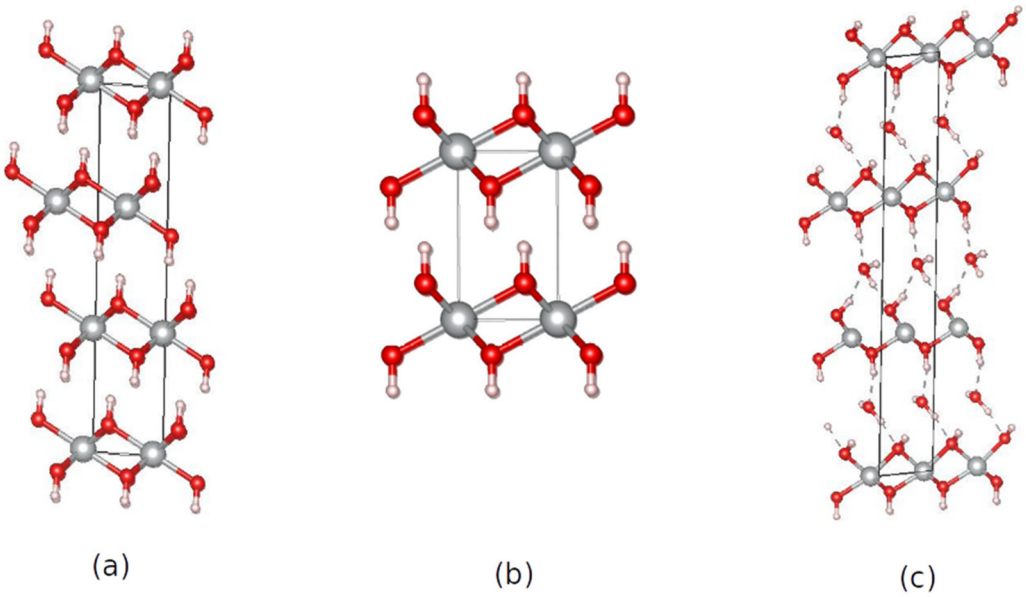

Fig. 7 The DFT-optimized geometries of (a) pristine α-$Ni(OH)_2$ with lattice constants 3.251, 3.252, 14.651 Å, (b) β-$Ni(OH)_2$ with lattice constants 6.392, 3.175, 4.664 Å and (c) water intercalated α-$Ni(OH)_2$ with lattice constants 3.231, 3.1, 22.263 Å. Atomic color code: Ni = grey, O = red, H = white.

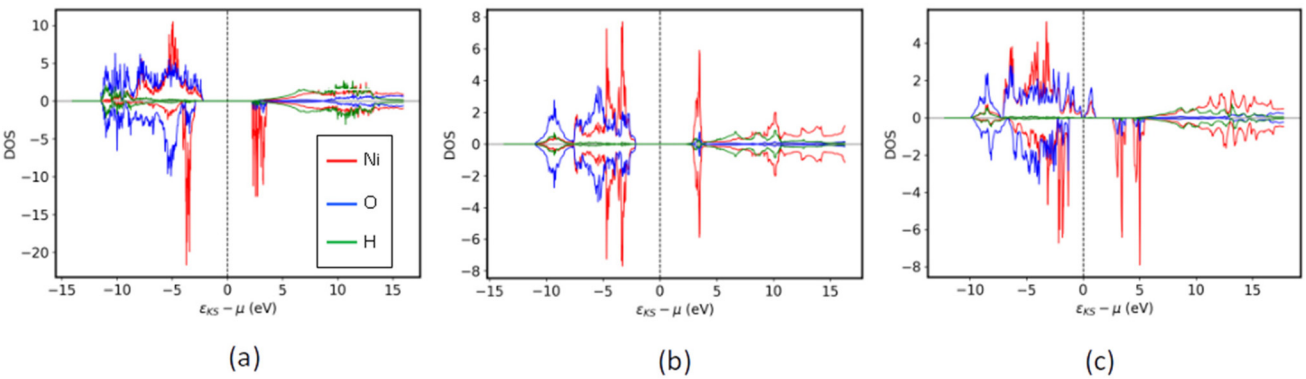

Fig. 8 The projected density of states (PDOS) of (a) water intercalated α-$Ni(OH)_2$, (b) pristine β-$Ni(OH)_2$ and (c) defected β-$Ni(OH)_2$ structures obtained from DFT-HSE06 calculations. The x-axis represents the energy measured with respect to the Fermi level and *y*-axis represents the DOS. The states corresponding to different atoms (spin up and down) are labelled.

We also evaluated the formation energies of both structures using the chemical potentials of bulk Ni, molecular O_2 and H_2O as references. The calculated formation energies for pristine α-$Ni(OH)_2$ and β-$Ni(OH)_2$ are the same within the computational accuracy, −0.261 eV per atom and −0.265 eV per atom, respectively. The negative formation energies indicate that both phases are thermodynamically stable and consistent with their experimental synthesizability. Upon water intercalation, the α-$Ni(OH)_2$ structure exhibits a more negative formation energy of −0.296 eV per atom, reflecting enhanced stability relative to the pristine phase. The intercalation energy per water molecule is calculated to be −1.063 eV, further confirming the stabilizing effect of water incorporation. The formation of the three strong hydrogen bonds in our intercalation model structure is related to an average hydrogen bond energy of 0.35 eV, surpassing the average hydrogen bond energy in liquid water.

To understand their electronic structure, projected density of states (PDOS) calculations were performed using DFT-HSE06 method. The PDOS of both α-$Ni(OH)_2$ and β-$Ni(OH)_2$ and a defective model β-$Ni(OH)_2$ of are shown in Fig. 8. The α-$Ni(OH)_2$ and β-$Ni(OH)_2$ have HSE06 band gaps of 4.37 and 4.24 eV, respectively. In both the phases, the valence and conduction bands have major contributions from Ni and O atoms. These values are significantly higher than the corresponding DFT-PBE values of 0.71 and 1.21 eV, respectively due to the well-known underestimation of band gaps by GGA methods. It is also noted that while α-$Ni(OH)_2$ is magnetic

with a total magnetic moment of 6 μB, β-$Ni(OH)_2$ is non-magnetic. Since both α- and β-$Ni(OH)_2$ exhibit relatively large band gaps, we explored whether introducing a defect by removing a H atom from the –OH groups could activate these structures as electrocatalysts, as one possibility of defect/dopants engineering. To investigate this, we introduced one –H vacancy in the unit cell of the β-$Ni(OH)_2$ structure, resulting in a 25% defect ratio, which may be somewhat too high for experimental purposes, but is a good and computationally feasible starting model. The PDOS for the defected structure is shown in Fig. 8c. As observed, the defect β-$Ni(OH)_2$ exhibits only a negligible band gap of 0.19 eV, indicating that it can facilitate electrocatalytic reaction. This electronic behavior suggests that defected structures in general are capable of supporting both urea oxidation and oxygen evolution reactions, consistent with experimental observations.

Conclusions

This study explored the role of $Ni(OH)_2$ phases in wastewater electrolysis for the sustainable production of green hydrogen, with focus on the OER and UOR. It was demonstrated that the best performing $Ni(OH)_2$ sample in OER was the one consisting as a mixture of the α- and β-$Ni(OH)_2$ phase (αβ1-$Ni(OH)_2$). This interfacial effect between the α and β phase was responsible for the sample's enhanced electrocatalytic activity, and reaction kinetics, compared to the single phase $Ni(OH)_2$ samples. αβ1-$Ni(OH)_2$ exhibited the smallest Tafel slope equal to 18.8 mV dec^{-1}, along with an potential of 1.42 V *vs.* RHE at 10 mA cm^{-2}, 1.63 V *vs.* RHE at 100 mA cm^{-2}, and 1.82 V *vs.* RHE at 500 mA cm^{-2}. The same sample was selected for further electrocatalytic evaluation in UOR. The αβ1-$Ni(OH)_2$ sample showed slower UOR reaction kinetics in comparison to OER, with a Tafel slope equal to 31.5 mV dec^{-1}. The potential for UOR at 10 and 100 mA cm^{-2} current densities was 1.40 and 1.60 V *vs.* RHE respectively, lower in comparison to 1.42 and 1.63 V *vs.* RHE for OER correspondingly. This means that less energy is required to run the UOR at those values of current density in comparison to OER. At higher current densities, higher than 100 mA cm^{-2}, the potential of the αβ1-$Ni(OH)_2$ sample at 500 mA cm^{-2} was 2.20 V *vs.* RHE for UOR, whereas for OER was 1.82 V *vs.* RHE for the same current density. Showing the complexity of UOR at such current densities since the reaction competes with OER, as both reactions utilise the same or similar active species. SEM and XPS analysis of the αβ1-$Ni(OH)_2$ sample after stability testing in OER showed that the sample's surface had both morphologically and chemically changed after applying chronoamperometry measurements for 24 h. Cracking and sintering of the sample's surface was evident, as well as chemical shifting and formation of oxygen defects. Contrary to this, the same sample showed no morphological degradation after its stability testing in UOR and no chemical oxidation on its surface. Whereas DFT studies, showed that defect formation in the $Ni(OH)_2$ crystal structure can enhance electron mobility resulting in enhanced OER and UOR activity. Providing valuable information in the design and interfacial engineering of $Ni(OH)_2$ electrocatalysts for wastewater electrolysis. Further in-depth computational studies of the αβ1-$Ni(OH)_2$ sample, operando Raman or DRIFTS spectroscopy are required in order to study how the percentage of the α and β in the $Ni(OH)_2$ influences the electron transfer as well as the binding and release of reactants and intermediates in OER and UOR. In addition, direct product identification by mass spectroscopy, gas chromatography or ion chromatography could further strengthen mechanistic interpretation of UOR. Last, conducting all electrochemical measurements trice should be considered in future work in order to enable rigorous statistical treatment in line with established validation guidelines.

Author contributions

All authors contributed at the writing of this manuscript and given approval to the final version.

Conflicts of interest

There are no conflicts to declare.

Data availability

The majority of the data supporting this article have been included as part of the supplementary information (SI). Supplementary information: additional materials characterizations and electrochemical measurements. See DOI: https://doi.org/10.1039/d5nr05037e.

Additional data that support the findings of this work are available from the corresponding author upon reasonable request.

Acknowledgements

M. V. S. acknowledges the financial support from the UCD Ad Astra fellowship programme, the UCD College of Engineering and Architecture Career Development Award and the Royal Chemical Society for the Research Enablement Grant #72049. A. S. N. would like to thank the German Research Foundation (DFG) for their support through the Walter-Benjamin Fellowship Program (project No. 540316537). This work used computing resources from the North German Supercomputing Alliance (Project ID 20814). M. V. S., C. K., N. R. and B. P. acknowledge the financial support from the Una Europa Seed funding SF2501: An Interdisciplinary Alliance on Materials for Clean Energy (ALMATCLEAN).

References

1 UN climate change, https://www.un.org/en/climatechange/science/causes-effects-climate-change. (accessed 29/11/2025).
2 W. Zhu, X. Fu, A. Wang, M. Ren, Z. Wei, C. Tang, X. Sun and J. Wang, *Appl. Catal., B*, 2022, **317**, 121726.
3 L. Qiao, A. Zhu, D. Liu, J. Feng, Y. Chen, M. Chen, P. Zhou, L. Yin, R. Wu, K. W. Ng and H. Pan, *Chem. Eng. J.*, 2023, **454**, 140380.
4 V. Vedharathinam and G. G. Botte, *Electrochim. Acta*, 2013, **108**, 660–665.
5 D. Zhu, C. Guo, J. Liu, L. Wang, Y. Du and S.-Z. Qiao, *Chem. Commun.*, 2017, **53**, 10906–10909.
6 Z. Li, Y. Zheng, H. Guo, X. Cheng, Y. Huang, C. Liu, J. Zang and L. Dong, *J. Alloys Compd.*, 2024, **1008**, 176591.
7 J. J. Medvedev, N. H. Delva and A. Klinkova, *ChemPlusChem*, 2024, **89**, e202300739.
8 S. Lu, X. Zheng, L. Fang, F. Yin and H. Liu, *Electrochem. Commun.*, 2023, **157**, 107599.
9 W. Yang, X. Yang, C. Hou, B. Li, H. Gao, J. Lin and X. Luo, *Appl. Catal., B*, 2019, **259**, 118020.
10 H. Qin, Y. Ye, J. Li, W. Jia, S. Zheng, X. Cao, G. Lin and L. Jiao, *Adv. Funct. Mater.*, 2023, **33**, 2209698.
11 Y. Li, F. Luo, Y. Xie, C. Chang, M. Xie and Z. Yang, *Int. J. Hydrogen Energy*, 2023, **48**, 9155–9162.
12 Y. Ye, Y. Gan, R. Cai, X. Dai, X. Yin, F. Nie, Z. Ren, B. Wu, Y. Cao and X. Zhang, *J. Alloys Compd.*, 2022, **921**, 166145.
13 Y. Mao, B. Zhou and S. Peng, *J. Mater. Sci.: Mater. Electron.*, 2020, **31**, 9457–9467.
14 Y. Li, J. Yao, Y. Zhu, Z. Zou and H. Wang, *J. Power Sources*, 2012, **203**, 177–183.
15 M. S. Akhtar, T. Wejrzanowski, G. Komorowska, B. Adamczyk-Cieślak and E. Choinska, *Electrochim. Acta*, 2024, **508**, 145284.
16 X. Yi, V. Celorrio, H. Zhang, N. Robertson and C. Kirk, *J. Mater. Chem. A*, 2023, **11**, 22275–22287.
17 L. Fei, H. Sun, X. Xu, Y. Li, R. Ran, W. Zhou and Z. Shao, *Chem. Eng. J.*, 2023, **471**, 144660.
18 A. Muthurasu, K. Chhetri, B. Dahal and H. Y. Kim, *Nanoscale*, 2022, **14**, 6557–6569.
19 P. C. Lohani, A. P. Tiwari, A. Muthurasu, I. Pathak, M. B. Poudel, K. Chhetri, B. Dahal, D. Acharya, T. H. Ko and H. Y. Kim, *Chem. Eng. J.*, 2023, **463**, 142280.
20 A. Kumar, X. Liu, J. Lee, B. Debnath, A. R. Jadhav, X. Shao, V. Q. Bui, Y. Hwang, Y. Liu, M. G. Kim and H. Lee, *Energy Environ. Sci.*, 2021, **14**, 6494–6505.
21 L. Guo, J. Chi, J. Zhu, T. Cui, J. Lai and L. Wang, *Appl. Catal., B*, 2023, **320**, 121977.
22 S. Brunauer, P. H. Emmett and E. Teller, *J. Am. Chem. Soc.*, 1938, **60**, 309–319.
23 E. P. Barrett, L. G. Joyner and P. P. Halenda, *J. Am. Chem. Soc.*, 1951, **73**, 373–380.
24 V. Blum, R. Gehrke, F. Hanke, P. Havu, V. Havu, X. Ren, K. Reuter and M. Scheffler, *Comput. Phys. Commun.*, 2009, **180**, 2175–2196.
25 J. P. Perdew, K. Burke and M. Ernzerhof, *Phys. Rev. Lett.*, 1996, **77**, 3865–3868.
26 J. Hermann and A. Tkatchenko, *Phys. Rev. Lett.*, 2020, **124**, 146401.
27 J. Heyd, G. E. Scuseria and M. Ernzerhof, *J. Chem. Phys.*, 2003, **118**, 8207–8215.
28 S. V. Chauhan, K. K. Joshi, P. M. Pataniya and C. K. Sumesh, *Sustainable Energy Fuels*, 2025, **9**, 3550–3576.
29 T. Shinagawa, A. T. Garcia-Esparza and K. Takanabe, *Sci. Rep.*, 2015, **5**, 13801.
30 M. Plevová, J. Hnát and K. Bouzek, *J. Power Sources*, 2021, **507**, 230072.
31 Y. Li, G. Tang, Y. Wang, Y. Chai and C. Liu, *ACS Omega*, 2022, **7**, 13687–13696.
32 R. Eloirdi, P. Cakir, F. Huber, A. Seibert, R. Konings and T. Gouder, *Appl. Surf. Sci.*, 2018, **457**, 566–571.
33 H. Liu, P. Wang, X. Qi, A. Yin, Y. Wang, Y. Ye, J. Luo, Z. Ren, L. Chen, S. Yu and J. Wei, *Molecules*, 2024, **29**, 3321.
34 X. Gao, X. Bai, P. Wang, Y. Jiao, K. Davey, Y. Zheng and S.-Z. Qiao, *Nat. Commun.*, 2023, **14**, 5842.
35 J. Zhang, J. Zhu, L. Kang, Q. Zhang, L. Liu, F. Guo, K. Li, J. Feng, L. Xia, L. Lv, W. Zong, P. R. Shearing, D. J. L. Brett, I. P. Parkin, X. Song, L. Mai and G. He, *Energy Environ. Sci.*, 2023, **16**, 6015–6025.
36 L. E. Krausfeldt, A. T. Farmer, H. F. Castro Gonzalez, B. N. Zepernick, S. R. Campagna and S. W. Wilhelm, *Front. Microbiol.*, 2019, **10**, 1064.
37 J. Zhang, X. Song, L. Kang, J. Zhu, L. Liu, Q. Zhang, D. J. L. Brett, P. R. Shearing, L. Mai, I. P. Parkin and G. He, *Chem. Catal.*, 2022, **2**, 3254–3270.
38 H. Sun, J. Liu, G. Chen, H. Kim, S. Kim, Z. Hu, J.-M. Chen, S.-C. Haw, F. Ciucci and W. Jung, *Small Methods*, 2022, **6**, 2101017.
39 V. Vedharathinam and G. Botte, *Electrocatalytic Oxidation Mechanism of Urea On Ni/Co Hydroxide Catalyst in Alkaline Medium*, 2013.
40 V. Vedharathinam and G. G. Botte, *Electrochim. Acta*, 2012, **81**, 292–300.
41 F. Guo, K. Ye, M. Du, X. Huang, K. Cheng, G. Wang and D. Cao, *Electrochim. Acta*, 2016, **210**, 474–482.
42 X. Zheng, J. Yang, P. Li, Z. Jiang, P. Zhu, Q. Wang, J. Wu, E. Zhang, W. Sun, S. Dou, D. Wang and Y. Li, *Angew. Chem., Int. Ed.*, 2023, **62**, e202217449.
43 H. M. Robin, H. Naha, Md. S. Hossain, Sk. Mashadul Islam Rafi, Md. Golam Kibria and M. Mourshed, *Energy Rev.*, 2025, **4**, 100155.
44 G. S. Cassol, C. Shang, A. K. An, N. K. Khanzada, F. Ciucci, A. Manzotti, P. Westerhoff, Y. Song and L. Ling, *Nat. Commun.*, 2024, **15**, 2617.